Post-Cold Frontal Clouds at the ARM Eastern North Atlantic site: An examination of the relationship between large-scale environment and low-level cloud properties

Catherine M Naud[1], James F Booth[2], and Fayçal Lamraoui[2]

[1]Applied Physics and Applied Mathematics, Columbia University/ NASA-GISS.

[2] Earth and Atmospheric Sciences, City University of New York - City College.

Corresponding author: Catherine M Naud (catherine.naud@columbia.edu)

Key Points:

- Post-cold frontal cloud at the ARM Eastern North Atlantic site are on average thicker, higher, and colder than clouds in non-post-cold front subsidence periods
- Weaker inversions and stronger surface temperature contrast help explain post-cold frontal cloud characteristics
- Low-level cloud boundaries are strongly correlated with the cold air outbreak parameter M in all subsidence periods at the ENA

This article has been accepted for publication and undergone full peer review but has not been through the copyediting, typesetting, pagination and proofreading process which may lead to differences between this version and the Version of Record. Please cite this article as doi: 10.1029/2018JD029015

Abstract

Using cloud and environment observations from the Atmospheric Radiation Measurement program Eastern North Atlantic site and an automated cold front detection routine, cloud properties in post-cold front (PCF) periods are examined and compared to similar conditions of subsidence (non-PCF). PCF periods exhibit stronger subsidence and wind speed than non-PCF periods, with weaker inversions and stronger surface temperature contrasts. Low-level clouds are predominant and are found to have higher cloud-base and top heights, colder cloud-top temperature, as well as greater vertical extent and liquid water path during PCF than non-PCF periods. The environmental metric that is best correlated with cloud boundaries for both PCF and non-PCF periods is the difference in potential temperature between the sea surface and 800 hPa, a parameter used to locate cold air outbreak conditions. However, the cloud vertical extent and liquid water path are found to be better correlated with sea-air temperature contrast, a parameter related to turbulent surface fluxes. The strength of the relationships between the cloud characteristics and these metrics does not differ for PCF and non-PCF periods. However, the strength of the metrics differs between PCF and non-PCF periods and can explain cloud property differences. The results suggest both the properties of the boundary layer and the presence of an upper-level cyclone associated with the cold front determine PCF cloud properties.

1 Introduction

General circulation models (GCMs) have difficulties representing the correct amount of clouds in the cold sector of extratropical cyclones (Bodas-Salcedo et al., 2012; 2014). This is also a problem in reanalyses and seems most acute in the wake of cold fronts, i.e., post-cold frontal (PCF) regions, (Naud et al, 2014). The PCF regions are populated by low-level

clouds, which are ubiquitous in marine environments globally (e.g. Tselioudis et al., 2000; Mace, 2010; Haynes et al., 2011). In the extratropics, it is well known that low-level clouds tend to be organized into open- and closed-cellular convection regimes (e.g., McCoy et al. 2017), however, less is known about how cold-season macroscopic cloud properties (e.g., cloud-base height) vary with atmospheric conditions. To our knowledge, PCF cloud observations have not been specifically documented and examined, and such a task is a necessary first step towards improving the representation of PCF clouds in GCMs.

Here we use ground observations from the Atmospheric Radiation Measurement (ARM) program Eastern North Atlantic (ENA) site (Wood et al, 2015) to explore the relationship between cloud properties and the large-scale environment in post-cold frontal conditions. The site, located on Graciosa Island in the Azores archipelago, presents the advantage of being maritime, at a latitude that sees cold frontal passages, and in a mostly pristine environment (Remillard et al., 2012; Pennypacker and Wood, 2017). Consequently, for its location, representativeness (e.g. Ahlgrimm and Forbes, 2014) and wide breadth of measurements, the ENA site is ideally suited to study low-level clouds.

This work will utilize ground measurements, radiosoundings and the Modern Era Retrospective analysis for Research and Applications version 2 (MERRA-2; Gelaro et al., 2017) to examine PCF periods. However, to identify important circulation features associated with the extratropical cyclone and cold front, we compare the atmosphere properties during PCF periods with time periods with subsidence but no cold front ("non-PCF" periods; defined in full in Section 2). The results focus on differences between PCF and non-PCF periods in terms of: 1) the large-scale environment, and 2) cloud property distributions. These differences then provide context for our analysis of the main drivers of cloud properties in PCF and non-PCF periods to help determine if there are unique cloud characteristics within extratropical cyclone cold sectors.

2 Observations and methodology

In this section, we detail the observations collected at the ARM ENA site, and describe the metrics used to characterize the large-scale environment as well as the methods used to identify PCF and non-PCF periods. In addition, we describe the binning methodology used to examine potential correlations between cloud properties and the large-scale environment.

2.1 Observations from the ENA site

For the ENA site, there are two distinct periods of observations that use similar instruments and measurements: the Clouds, Aerosols, and Precipitation in the Marine Boundary Layer (CAP-MBL; Wood et al., 2015) experiment from 2009-2010, and the operational period from 2014-present (here we use data up to the end of 2017). For each of these periods, we use the meteorological station observations that collect, at a 1-minute time interval, near surface observations of temperature, wind direction and speed, pressure and humidity (ARM, 2013a).

We also utilize radiosoundings that have profiles of temperature, pressure, wind, and humidity (ARM, 1993). During the operational period, unless there is a field experiment, the soundings are launched twice daily. During CAP-MBL and during the Aerosols and Cloud Experiment in the Eastern North Atlantic campaign in June-July 2017 and January-February 2018, radiosondes were launched 4 times daily.

Cloud liquid water path (LWP) and column integrated precipitable water (PW) are obtained every 10 seconds with the microwave radiometer (MWR; ARM, 2009b, 2014a). Cloud-base heights and cloud-top heights can be obtained from two different products: 1) they are retrieved every 30 seconds using the micropulse lidar (MPL; Wang and Sassen, 2001; ARM, 2013b) and 2) every 10 seconds using the Active Remote Sensing of CLouds

(ARSCL; ARM, 2009a, 2015) algorithm (Clothiaux et al., 2000; Kollias et al., 2007). The MPL product does not sample the atmospheric column below 500 m, so some cloud-base heights can be artificially placed at this level, while the reported Cloud Base Best Estimate found in the ARSCL files is based on both the ceilometer and MPL and does not suffer from this issue. However, the 95 GHz radar that is at the core of the ARSCL algorithm was not deployed at the ENA before July 2015 which significantly limits the amount of data at our disposal. Nevertheless, because of its greater accuracy, for consistency we will use the ARSCL cloud-base, cloud-top and cloud vertical extent products. The MPL cloud-top heights will be used to test the robustness of our results in section 4, in addition to the ceilometer cloud-base height estimates (ARM, 2009c, 2013c; Clothiaux et al., 2000). We acknowledge that for a number of these data products, precipitation might be a problem, either by causing attenuation of the measurements (e.g. MPL) or by affecting the instruments as they get wet (e.g. MWR). We will thus discuss this issue in section 3.2, based on observations from the meteorological station optical rain gauge (ARM, 2013a) and the laser disdrometer (ARM, 2014b).

All these instruments and products have different temporal resolutions. To reconcile this issue, we use the radiosonde launches as the time of reference: the meteorological station data is extracted for the time that matches the sounding launch, which we found to have minor impacts compared to an average of ascent duration given that we focus on low clouds; the ARSCL and other cloud boundary data are collected through the hour centered on the launch and the median value of cloud-base, top height and cloud vertical extent are estimated; the mean LWP and PW when positive during the same hour are calculated. Consequently, for the majority of the study, we will use twice daily data points.

2.2 Environment metrics

To derive measures of the environmental conditions, we supplement surface and sounding observations with the MERRA-2 reanalysis (GMAO, 2008). The MERRA-2 hourly 0.5 °x 0.67° fields that we select are: 500 hPa vertical velocity to characterize the subsidence strength (ω), the skin temperature and sea level pressure to obtain the potential temperature at the sea surface (θ_{skin}), and the precipitable water (PW). For all these fields, we select the hourly time step closest to the radiosonde launch time. We find a decent agreement between MERRA-2 and the MWR hourly mean of PW (mean difference = 0.5±4.1 mm, R=0.83), giving us confidence that the MERRA-2 output represents realistic conditions at the site.

To characterize the dynamics, moisture, surface forcing, and static stability of the PCF environment we chose the following metrics: subsidence strength (ω), surface wind speed, sea-air temperature contrast (ΔT_{surf}), estimated inversion strength (EIS; Wood and Bretherton 2006), the marine cold air outbreak (MCAO) parameter M (Fletcher et al., 2016a), the surface relative humidity (RH_{surf}) and the PW. Table 1 provides formulas and indicates which datasets are used for each metric. Of all parameters, the calculation of EIS necessitates the most observations: the 700 hPa potential temperature θ_{700} is obtained with the radiosounding; the potential temperature of the surface air θ_{surf} is obtained from the meteorological station; the adiabatic lapse rate at 850 hPa ($\Gamma_m^{850)}$) is calculated with the formula given in Wood and Bretherton (2006) and makes use of the 700 hPa temperature from the radiosounding and the surface air temperature from the meteorological station, the 700 hPa geopotential height Z_{700} is from the radiosounding; the lifting condensation level (LCL) is calculated with the surface meteorological station temperature and assumes a relative humidity RH=80% (again as in Wood and Bretherton, 2006).

This choice of metrics is in part motivated by relationships that have been established for subtropical clouds in the absence of cold fronts. The expected impact of each of these metrics

is summarized in Table 1. Some of these parameters are chosen based on previous work on low-clouds in midlatitude regions. For example, both surface wind speed and surface temperature contrast act as a proxy for surface sensible heat flux, which are known to impact boundary layer stability and low-level cloud fraction (e.g. Miyamoto et al., 2018). EIS is analyzed because of the importance of an inversion in the lower troposphere for ocean boundary layer clouds (e.g. Wood 2012). In PCF regions, cloud fractions were found to be well correlated with EIS (Naud et al., 2016). Strong inversions help maintain well mixed cloud topped boundary layers in stratocumulus decks by containing the atmospheric moisture near the surface. Weaker inversions cause a decoupling in the boundary layer, its deepening and the presence of cumulus clouds (e.g. Bretherton and Wyant, 1997). The marine cold air outbreak parameter M has been shown to delineate between two common regimes for shallow clouds globally: as M increases the frequency of open cells increases while the frequency of closed cells decreases (McCoy et al. 2017).

2.3 Identification of post-cold frontal periods

In order to identify PCF periods, we first use a cold front location database (Naud et al., 2016) to shortlist dates with a possible cold front passage at the ENA site. The database identifies cold fronts associated with an extratropical cyclone every 6-hours using MERRA-2 temperature and wind output. Because the method cannot always identify a cold front as the storm evolves, or the full extent of the front, and because the identification only occurs every 6 hours, we keep cases for which a cold front is identified in any of the following configurations: just east of the site, just west of the site, on both sides of the site within 6 hours, or within 2500 km of the site, on either side. The resulting shortlist includes ~1800 cases for the full 7 years considered here (i.e. 2009-2010 and 2013-2017), regardless of whether there were ground-based observations performed at the time.

This shortlist of cases is then refined using the time series of ENA wind direction from the meteorological station. On the dates when meteorological observations are available and a potential cold front passage is tentatively identified, we apply a 1-hour moving window smoothing function on the wind direction measurements and then test for a shift in wind direction from southerly to northerly at the site. If such a condition occurs, we keep the case. The time at which the wind direction changes marks the start of the PCF period. Then the PCF periods are deemed terminated when the wind becomes southerly again.

Using this method, for the two time periods with observations (2009-2010 and 2013-2017) we identified 80 cases for which PCF periods occur at the ENA site. The full list of candidate PCF dates is given in appendix A with start time and duration. Here we only keep the 77 cases for which the PCF periods last at least 2 hours: 24 cases in winter, 19 in the spring, 15 in summer, and 19 in the fall. The duration varies between a little over two hours and just under 6 days, with a median value of about 28 hours. For these 77 cases, there are 280 radiosonde launches, and therefore, this is the number of PCF data points available.

2.4 Identification of non-PCF periods

To contrast cloud and environmental properties between post-cold front periods and periods where low-level clouds occur but not under the influence of an extratropical cyclone, we propose the following simple classification for all situations where subsidence is diagnosed with MERRA-2 (i.e. $\omega_{500} > 0$ hPa hr^{-1}): 1) "PCF" periods as defined above, i.e. cold front identified and northerly winds; 2) no cold front identified and northeasterly winds, referred to as "non-PCF-north" (in this case northwesterly winds are not included to avoid possible contamination when cold fronts are present but could not be identified); and 3) the winds are southerly, referred to as "non-PCF-south". The choice of subsidence is because PCF periods are dominated by subsidence.. Compared to PCF periods, there are a larger number of radiosonde launches available during non-PCF periods for the two epochs of

observations at the ENA site. A total of 615 launches/data points were available for non-PCF-north periods and 669 for non-PCF-south periods. We tested our results by randomly halving the number of non-PCF data points and find no significant difference (not shown).

2.5 Data points binning

In our analysis, the observations are from multiple sources, with different time resolutions and measurement uncertainties, consequently we expect some amount of scatter. In addition, most relationships with large-scale metrics examined here were first introduced for quantities averaged over long periods of time and/or large areas. Here the data points are near instantaneous and for a single location. Therefore, to reduce the signal-to-noise ratio in our examination of the relationships between large scale and cloud properties, we average the cloud observations for ranges of values of the large-scale metrics. This is achieved as follows: for each metric separately, we sort the data points and arrange them in a series of bins of equal range. Then we average in these bins cloud parameters and/or the other metrics. We impose that each bin contains at least 5 data points. We then examine the correlation coefficients between the variable on which the sorting is based, and all the other variables arranged and averaged in these bins. Note that the binning considers all data points to be independent, they are not intentionally grouped per date, but by large-scale metric value. The choice of bin size is arbitrary but ensures that there are a reasonable number of bins (at least 10), and enough data points per bin to exceed the minimum of 5 that is imposed (no more than 25 bins). When the data is sorted based on EIS, the bin size is chosen to be 2 K, 0.5 K for ΔT_{surf}, 1 ms^{-1} for surface wind speed, 3 K for M, 0.5 hPa hr^{-1} for the vertical velocity, 5% for RH_{surf} and 2 mm for PW.

3 Results

To discern the role of the extratropical cyclone circulation in impacting the clouds, we compare large-scale circulation and cloud characteristics during post-cold frontal periods (PCF) with those during times with similar subsidence and large-scale horizontal winds, but no cold front (i.e. non-PCF). The first analysis focuses on the large-scale conditions for the three categories (i.e. PCF, non-PCF-north and non-PCF-south) using the metrics listed in section 2.2. The second analysis considers the clouds characteristics. Then we investigate relationships between the large-scale metrics and the cloud properties.

3.1 Large-scale conditions

During most of the year, the large-scale wind patterns over the ENA site are associated with a semi-permanent subtropical anticyclone (e.g., Wood et al. 2015). Based on composites of MERRA-2 sea level pressure (SLP) during PCF periods, an anticyclone is often present right after a cold frontal passage as well (Figure 1a). These surface high-pressure systems travel west-to-east behind cold fronts: Figure 2 illustrates the advance of a high pressure system between the time of a cold front passage at the ENA site and 12 hours later. Consequently, even when the wind direction at the site in northwesterly, the site might be affected by advection associated with an upstream anticyclone. Depending on the position of the anticyclone relative to the cold front, the wind direction at the site can also be northeasterly. Overall, 2/3rd of all radiosonde launches display a northwesterly wind direction at the site during PCF periods (recall PCF periods begin with a shift from southerly to northerly). In fact, we find that even if the wind is northeasterly when PCF periods are identified, the large-scale metrics at the site resemble those of northwesterly wind PCF periods more than the conditions of non-PCF-north periods (not shown). Therefore, we have chosen to include northeasterly wind situations in our classification of PCF periods.

The composites suggest varying levels of influence from the surface anticyclone, ranging from: (i) a shared influence with the cold front's parent cyclone in PCF periods (Figure 1a); (ii) the anticyclone encompasses the site in non-PCF-north periods as its center travels north of the ENA site (Figure 1b); and (iii) the anticyclone travels south of the ENA site instead in non-PCF-south periods (Figure 1c).

Focusing on the differences between PCF and non-PCF periods, we now turn to the large-scale properties using the metrics listed in section 2.2. The subsidence is stronger overall (Figure 3a) and surface wind speeds reach larger values during PCF periods (Figure 3b). Thus, the sorting of dynamical variables suggests that PCF periods involve more vigorous vertical and lateral motion. The main distinction between non-PCF-north and non-PCF-south comes from the subsidence strength, as it is even weaker in non-PCF-south periods than both PCF and non-PCF-north periods. Interestingly, when examining the lower troposphere stability, the EIS distribution appears slightly bimodal during PCF periods (Figure 3c). This suggests two regimes for the strength of the inversion during PCF periods, one that matches what is found for non-PCF periods where EIS peaks at ~ 5 K, and the other below 0 K that tails to much smaller values, i.e. weak inversion conditions occur more often during PCF than non-PCF periods. The distribution of EIS in non-PCF-north periods suggests a greater (lower) propensity for strong (weak) inversions than in both PCF and non-PCF-south periods. The MCAO M parameter is considered to indicate marine cold air outbreak conditions when positive. In fact, neither PCF nor non-PCF periods have many cases with $M > 0$ but M is larger, i.e., closer to MCAO conditions, in PCF compared to non-PCF periods (Figure 3d). However, in contrast with the EIS distributions, the M distribution suggests greater instability in non-PCF-north than non-PCF-south periods. The surface temperature contrast ΔT_{surf} distribution (Figure 3e) mirrors M, i.e. stronger instability ($\Delta T_{surf} > 0$) in PCF than non-PCF-north than non-PCF-south periods. Both measures of PW (Figure 3f for MERRA-2, MWR

not shown) indicate rather dry conditions for both PCF and non-PCF periods, albeit with slightly more of the drier cases in PCF periods. Non-PCF-south periods are surprisingly not those with the largest PW. Finally, PCF periods also exhibit low RH_{surf} values more often than non-PCF periods with non-PCF-south displaying the largest values (Figure 3g). To summarize, PCF periods are more dynamically active, drier and more unstable than their non-PCF counterparts, while conditions of subsidence with southerly winds are the most quiescent, moist and to some extent stable of the three synoptic categories.

3.2 Statistical analysis of cloud properties

Because the cloud property datasets are time series, we can derive the frequency of cloud occurrence over the site during PCF and non-PCF periods. From the time series of ARSCL cloud-base heights, we find that a cloud is detected 88% of the time during PCF periods, 87% in non-PCF-north and 79% in non-PCF-south periods. This frequency of cloud occurrence is less when we use the MPL cloud mask instead, down to around 60%, possibly due to differing sensitivity, resolution and length of measurements epoch. However, when clouds are detected, both datasets agree that low-level clouds (with a top below 3 km) dominate and constitute about ¾ of all clouds that are detected. Therefore, we now only consider periods where ARSCL cloud-top heights are found below 3 km. One possible issue that can affect cloud retrievals is precipitation, as mentioned in 2.1, although this would be a very minor issue for ARSCL. Both rain-gauge and laser disdrometer products indicate that at the most, precipitation occurs 6% of the time in PCF periods, while it only occurs 2-3% of the time in non-PCF-south periods. This suggest that contamination of cloud products by precipitation should be minimal for this analysis.

Focusing first on cloud-base height distributions, clouds tend to have a cloud base below 1 km, with a peak around 0.5-0.7 km for all three categories (Figure 4a). However, the PCF cloud-base distribution shows a secondary peak at higher altitude, ~ 1.3 km. Cloud-base

height distributions are very similar for non-PCF-north and non-PCF-south periods. The PCF cloud-top height distribution also displays two peaks, one just below 1 km and the other closer to 2 km, while the non-PCF cloud tops peak somewhere in between around 1-1.5 km (Figure 4b). Similarly, PCF cloud-top temperatures display two peaks, while non-PCF distributions only display one, around 282 K (Figure 4c). Consequently PCF cloud tops are more often found in the mixed phase zone with temperatures less than 273.15 K. The PCF periods tend to have more of the thicker clouds as compared to the non-PCF periods (Figure 4d) but overall all three synoptic categories display very similar cloud vertical extent distributions. Finally, the liquid water path distribution indicates more of the larger LWP cases occur in PCF than non-PCF periods. To summarize, PCF clouds are higher, deeper, colder and with larger liquid water amount than their non-PCF counterparts. Next we examine the possible reasons for these differences in cloud properties.

3.3 Cloud properties versus environmental conditions

Here, we explore the relationship between cloud properties and EIS, ΔT_{surf}, M, wind speed, RH_{surf}, PW and subsidence strength. For this analysis, we sort the data using the environmental parameter bins described in section 2.5 and average the cloud properties in each bin. Table 2 summarizes the correlation coefficients between the environmental metrics and cloud properties, for PCF and non-PCF periods, using ARSCL for cloud boundaries. We focus on those coefficients that indicate significant relationships (at the 99.95% level).

Two metrics show a significant correlation with cloud-base height for all three categories: M and RH_{surf}. Figure 5 shows the relationship using all data points as well as the fixed size bins averages used in Table 2. As M increases so does the base height, suggesting that the boundary layer deepens. At the same time the inversion weakens (EIS is inversely correlated with M; this is explored in Section 4), overall causing clouds to form at higher altitude, consistent with the transition from a well-mixed to a decoupled planetary boundary

layer (e.g. Wood 2012 and references therein). This transition is accompanied by a decrease in RH_{surf} near the surface, which explains the inverse correlation between RH_{surf} and cloud-base height. M can be larger in PCF than non-PCF periods, which can explain the higher cloud base in the PCF periods. At the temporal and spatial resolutions used here, M seems to be a good predictor of cloud-base height.

Cloud-top heights are also strongly correlated to M for all three categories, and inversely correlated to EIS (Table 2), although there is more scatter when examining the relationship with EIS (Figure 6) and the correlation in PCF periods is not significant at the 99.95% level. In contrast, cloud-top temperatures show a significant correlation with a number of metrics, namely M, EIS, ΔT_{surf}, PW and wind speed in PCF and non-PCF-north periods, or M, ω, RH_{surf} and PW in both on-PCF periods (Table 2). As M increases, or EIS decreases, or ΔT_{surf} increases, both weakening inversion and strong surface forcing cause the cloud-top temperatures to decrease (Figure 7). In PCF periods, we observe a propensity for clouds to reach colder temperatures because of a larger frequency of occurrence of weak inversions, dry conditions, and strong surface temperature contrast as well as stronger winds. We note a much clearer relation between M or EIS and cloud-top temperature as compared to cloud-top height (c.f. Figure 6), possibly because cloud-top temperature is calculated from the same radiosounding that is used for calculating M and EIS. We also note that for non-PCF-south, although the inverse correlation coefficient is large, it is not significant to the highest level. Nevertheless, out of all the metrics tested here, M tends to display a strong relationship with cloud boundaries overall that is consistent across the three type of synoptic conditions (Figures 5-7). In addition, given the propensity for M to be larger in PCF than non-PCF periods, this relationship can help explain the tendency for clouds to be higher in PCF periods.

Cloud vertical extent has a much lower correlation with the metrics considered here as compared to cloud-base or top heights, and only a few are in fact significant at the 99.95% level. However, M, RH_{surf} and ΔT_{surf} show some degree of correlation with cloud vertical extent, for both PCF and non-PCF, albeit with a significance above the 99.95% for PCF only for RH_{surf}, and for non-PCF-north only for ΔT_{surf}. None are at this significance level for non-PCF-south, but the correlation coefficient is large for both M and RH_{surf}. The cloud vertical extent is larger in PCF than non-PCF periods regardless of RH_{surf} values (Figure 8a). Also, the relationship with RH_{surf} might be more sigmoid than linear. The relationship with ΔT_{surf} is also rather noisy, but seems to be linear and virtually identical in PCF and non-PCF-north periods (Figure 8b). It is not though for non-PCF-south, suggesting that the relationship between ΔT_{surf} and cloud vertical extent is mostly relevant in conditions akin to cold air outbreaks (i.e. positive ΔT_{surf}). Despite the weaker correlation with M in all periods, the vertical extent is linearly related to M but the clear disconnect between the binned data fit and the location of most data points in Figure 8c casts some doubts as to the robustness of such a relationship. These results suggest that cloud vertical extent depends more on the surface forcing than the strength of the inversion, and but this is only true for northerly wind conditions.

The correlation coefficients in Table 2 suggest that the logarithm of LWP is not linearly related to the metrics tested here overall, although some level of correlation is found in the mean for RH_{surf}, M and ΔT_{surf}. Figure 9a suggests that although LWP shows a similar relationship with RH_{surf} in PCF and non-PCF, overall it is slightly larger in PCF than non-PCF regardless of RH_{surf}. This is what we had also found when examining the relationship between vertical extent and RH_{surf}. The bin-averaged fit for both ΔT_{surf} and M is rather linear (Figures 9b,c), at least for the northerly wind conditions, but the relationship between LWP and ΔT_{surf} appears more robust than with M. This can explain the larger LWP values in PCF

periods. As is the case for the cloud vertical extent, the relatively larger correlation coefficients in Table 2 suggest that the surface forcing is the main driver for LWP.

To summarize for all situations of subsidence at the ENA site, we find that the best predictor of cloud-top height and temperature is M, and this parameter is also a good predictor of cloud-base height. For cloud vertical extent and liquid water path, the surface forcing given by ΔT_{surf} is the best predictor of all the metrics tested here, but the relationship is noisy. Regarding specifically PCF conditions, the impact of extratropical cyclones on cloud boundaries and liquid water path seems to be an enhancement of the temperature contrast between the advected air and the surface temperature, as compared to more quiescent conditions. This helps to both increase the surface forcing and weaken the inversion (and lower the tropospheric stability). These changes favor a decoupled boundary layer and both higher and thicker clouds than in more quiescent conditions.

4 Discussion

In the previous section, two results emerged that require some further investigation: 1) PCF clouds respond to large-scale forcings similarly to less dynamically active subsidence conditions; and 2) the M parameter correlates well with low-level cloud boundary locations in subsidence conditions. Here we want to 1) test how robust these results are with respect to observational uncertainties, 2) analyze how M might relate to other of the large-scale metrics considered here in order to understand better why it shows such strong correlations with cloud boundaries.

4.1 Sensitivity to observational uncertainties

With the datasets at our disposal, we cannot test the sensitivity to the large-scale metrics information, but we can still explore the impact of using different datasets for the cloud boundaries. Here we only consider PCF and non-PCF-north periods for simplicity. A first test

concerns the differences in cloud boundary distributions between PCF and non-PCF periods discussed in section 3.2. For this, we compare PCF and non-PCF distributions of cloud-base height obtained with the ceilometer and cloud-top height and temperature obtained with the MPL cloud mask product. We discussed earlier that the MPL based cloud mask does not report cloud-base height below 500 m, so for this cloud boundary we test our results with the ceilometer data. The latter is not an ideal choice, because this product is used to determine the cloud-base height best estimate reported in ARSCL, but this product has the advantage of being available over a much longer period than ARSCL. This implies that for both the MPL and ceilometer data products, we can test as well the effect of sample size. Regardless of the choice of cloud dataset and/or sample size, the separation between PCF and non-PCF cloud boundaries persists: PCF clouds have high cloud-base and cloud-top heights, and reach colder temperatures (Figure 10).

Second we examine the relationships with the large scale metrics when using MPL rather than ARSCL for both cloud-top height and temperature and ceilometer for cloud-base height. Table 3 lists the correlation coefficients between the large-scale metrics and these alternate retrievals for both PCF and non-PCF-north periods. A comparison with the results reported in Table 2 indicates that regardless of the instrumentation used to obtain cloud boundaries, 1) cloud-base and top heights, and top temperature are all strongly correlated (inversely for temperatures) with M and 2) this strong relation is found for both PCF and non-PCF subsets. Not surprisingly, when using the ceilometer in place of the ARSCL best estimate for cloud-base heights, the correlation coefficients and significance for M and RH_{surf} are consistent in tables 2 and 3, albeit with the coefficients slightly weaker when using the ceilometer. When using MPL for cloud-top heights, the correlation coefficients for M are very close to those obtained with ARSCL, however, the correlation with EIS is stronger for PCF periods with MPL, and much weaker with PW for non-PCF-north periods. For MPL cloud-top

temperatures, most correlations found with ARSCL are still present, MPL just gives a more significant relation with RH_{surf} in PCF periods. Despite the differences found between tables 2 and 3, there seems to be a very marginal impact of the dataset used for cloud boundaries on our results: the strong relationship between cloud boundaries and M persists.

4.2 Relationship between M and the other large-scale metrics

To help understand why M proves to be such a robust driver of cloud boundaries in subsidence conditions at the ENA site, we explore its relationship with the other, more widely used for low-clouds, large scale metrics. This analysis provides context regarding which cloud-metric relationships might be causal, and at the same time it establishes how the large-scale metrics interact during PCF and non-PCF periods for the ENA site.

We use the binning approach defined in the methods section to calculate correlation coefficients between M and the metrics EIS, ΔT_{surf}, wind speed, RH_{surf}, PW and subsidence strength ω (Table 4). Table 4 includes the correlation coefficients for PCF and both non-PCF periods separately. For a relationship to be robust, the correlation should be significant to the 99.95% level for both PCF and non-PCF data points.

The most robust relationship is found between M and EIS, which are inversely correlated with coefficients of -0.98, -0.98 and -0.96 for PCF, non-PCF-north and non-PCF-south periods. This suggests that M is strongly related to the strength of the inversion. These results agree with the strong negative correlation between M and EIS in midlatitude stratocumulus cloud regions of McCoy et al. (2017). This agreement suggests the relationship is robust, because McCoy et al. (2017) focused on NASA Moderate Resolution Imaging Spectroradiometer (MODIS) swaths anywhere in the global oceans between 65°S and 65°N, whereas the present study uses single site observations for situations of subsidence aloft.

With lower coefficients and significance, across all three synoptic categories, the relationship between M and both PW and RH_{surf} also suggests that M might characterize the moisture availability in the boundary layer, possibly through the relationship between temperature and specific humidity. The coefficients are negative, suggesting that as the potential temperature contrast between the surface and the 800 hPa level decreases (i.e. M increases and ultimately becomes positive), the boundary layer becomes drier.

Interestingly, correlations are larger for the PCF and non-PCF-north than non-PCF-south periods between M and wind speed or M and ΔT_{surf}. This may result from surface sensible heat fluxes changing the skin temperature. From a bulk formula approach, the surface sensible heat flux is a function of wind speed (as well as air-sea temperature difference). Sensible heat flux influences the skin temperature, on which M is based, possibly causing an indirect relationship between wind speed and M. However, the fact that a relationship between M and either wind speed or ΔT_{surf} does not hold in non-PCF-south periods might suggest that it is specific to cold-air advection conditions, casting doubts in possible causality. It should be noted that McCoy et al. (2017) found that in open-cell cloud conditions M depends on both EIS and ΔT_{surf}, but only on EIS in closed-cell regimes.

Based on these results, the strong relationship we find between cloud boundaries and M might be because the latter informs on both inversion strength and moisture availability. In addition, the strong relationship in cold air advection situations (i.e. both PCF and non-PCF-north) between cloud vertical extent/LWP and ΔT_{surf} suggests the strong role of sensible heat fluxes in these synoptic conditions for these cloud properties.

5 Conclusions

Using observations from the ARM Eastern North Atlantic site in the Azores, this work examines clouds and their relationship with a number of environmental metrics in post-cold frontal (PCF) periods and periods of subsidence without the influence of an extratropical

cyclone (non-PCF). For this midlatitude maritime location, PCF periods are found to have larger subsidence strength and wind speed, stronger surface temperature contrast and more frequent weak inversions than their non-PCF counterparts. Clouds are found to be higher, colder, thicker and with larger liquid water path more often in PCF than non-PCF periods. We test different environmental metrics and find larger correlations with cloud boundary locations when using the parameter M (θ_{skin}-θ_{800hPa}): the larger M, the more unstable the boundary layer, the higher the cloud-base and top heights. Cloud vertical extent and liquid water path are better correlated with ΔT_{surf} (the sea-air temperature contrast): the larger the contrast, the thicker (in extent and opacity) the clouds; presumably because larger ΔT_{surf} generates larger surface sensible heat fluxes, driving more vigorous shallow convection. However, this potential process is not found in conditions of southerly winds (or warm air advection). Because both M and ΔT_{surf} are larger in PCF periods than non-PCF periods, together inversion strength and surface forcing cause the clouds to be thicker and higher in PCF periods. Processes internal to the boundary layer were diagnosed with RH_{surf} which also is found to be well related to cloud-base heights, as well as cloud vertical extent and LWP.

The strong correlation between M and cloud boundary properties offers a useful and rather simple metric to help in the evaluation of models in the midlatitudes. Our results align with those of McCoy et al (2017) and suggest that as conditions are more dynamic, the cloud organization transitions from closed to open cell. The results suggest that M is useful to better predict the cloud types and the boundary layer structure in subsidence conditions, and that M also helps explain the impact of the large-scale dynamics on these clouds.

The lower tropospheric stability (LTS) measure of Klein and Hartmann (1993) was an attempt to help diagnose the change in cloud cover expected for a change in sea surface temperature, but it had some shortcomings in the midlatitudes. The corrected measure proposed by Wood and Bretherton (2006), i.e. EIS, allowed a generalization of the relation

between cloud cover and lower tropospheric stability to all latitudes but also implied a diminished response of cloud cover to changes in temperature, with the introduction of the moist adiabat. Here, we find that EIS is still a valuable metric for the cold air advection conditions when examining cloud boundaries but M seems to be more robust. This said, McCoy et al (2017) also found that M was not well correlated with cloud spatial organization at low latitudes and so more work is needed to evaluate the usefulness of such a metric for GCMs, i.e. if it were to be used globally in a capacity similar to what was done with LTS (Köhler et al., 2011) or more recently with EIS (Zhao et al, 2018) to help better represent the transition between stratocumulus and cumulus clouds when boundary layers undergo decoupling.

The study herein is conducted at a single site in the north Atlantic. However, cloud characteristics from the site have been shown to be representative of low-level clouds globally at similar latitudes (Ahlgrimm and Forbes, 2014). An open question is whether these cloud characteristics change drastically at higher latitudes where PCF conditions are colder. Thus, the next step in our analysis will be to study observations from the Southern Ocean. This will be particularly informative as clouds there are more often supercooled than in the northern hemisphere (Morrison et al. 2011), extratropical cyclones are ubiquitous regardless of season, and the aerosol population rather different.

Acknowledgments, Samples, and Data

The work is funded by the U. S. Department of Energy office of science grant number DE-SC0016344 as part of the Atmospheric Systems Research program. The MERRA-2 files were obtained from the NASA Goddard Earth Sciences Data and Information Services Center https://disc.sci.gsfc.nasa.gov/. All ARM observations were obtained from https://www.archive.arm.gov/discovery/.

Appendix A

Table A1. List of post-cold frontal periods in chronological order: date in year, month, day (yyyymmdd), PCF start time on that date in decimal hours, and PCF duration (period with northerly winds) in decimal hours for 80 cases.

Case	Date (yyyymmdd)	Start time (decimal hours)	Duration (decimal hours)	Case	Date (yyyymmdd)	Start time (decimal hours)	Duration (decimal hours)
1	20090509	7.11667	44.2500	**2**	20090512	22.3500	23.3167
3	20090723	5.68333	19.0167	**4**	20090824	1.55000	24.1000
5	20090914	8.93333	82.5000	**6**	20091026	14.8500	10.0667
7	20091126	9.18333	23.5000	**8**	20091210	5.01667	36.7833
9	20100103	6.61667	24.4000	**10**	20100109	8.05000	19.6333
11	20100115	22.4167	2.53330	**12**	20100127	23.5000	1.56670
13	20100203	20.3667	18.3000	**14**	20100207	18.2500	7.93330
15	20100227	4.51667	19.3833	**16**	20100321	23.0000	1.01670
17	20100328	10.9667	34.7500	**18**	20101028	6.86667	29.7333
19	20101206	4.23333	136.550	**20**	20101212	5.83333	18.2000
21	20131020	17.0167	47.5500	**22**	20131122	9.61667	15.5666
23	20140102	4.31667	22.0666	**24**	20140111	4.18333	38.8500
25	20140115	0.833333	106.034	**26**	20140202	10.9667	24.4666
27	20140205	13.3000	28.0000	**28**	20140224	12.5333	13.6167
29	20140323	16.3167	19.7000	**30**	20140329	0.0833333	34.8167
31	20140409	9.51667	23.9333	**32**	20140415	9.68333	58.2000
33	20140418	14.4333	53.2000	**34**	20140605	2.96667	89.5166
35	20140626	20.3167	32.3333	**36**	20140721	20.9333	24.5500
37	20140817	17.6167	50.7166	**38**	20140831	7.76667	30.3333

39	20140914	16.4500	80.5833	**40**	20141110	4.50000	30.3167
41	20141123	13.3167	29.1000	**42**	20141125	13.5333	28.3500
43	20141127	9.03333	59.4334	**44**	20141212	8.00000	37.0667
45	20150104	22.3333	26.4834	**46**	20150302	18.0000	21.9333
47	20150311	16.6333	16.1334	**48**	20150411	12.4000	55.9500
49	20150415	6.75000	33.9833	**50**	20150422	2.11667	53.6666
51	20150603	23.8500	19.4833	**52**	20150804	6.40000	30.5167
53	20150828	1.43333	62.3334	**54**	20150921	9.21667	16.7500
55	20151028	14.0500	10.8500	**56**	20151107	14.4667	14.7833
57	20151123	23.7500	26.9667	**58**	20151212	7.25000	48.4333
59	20151224	20.9000	47.7667	**60**	20151231	15.7500	14.5500
61	20160225	19.2167	59.6500	**62**	20160313	19.0333	6.35000
63	20160408	14.6500	100.183	**64**	20160523	5.38333	111.667
65	20160621	3.50000	23.9667	**66**	20160626	23.9500	2.55000
67	20160628	7.91667	93.6503	**68**	20160718	13.8833	36.9167
69	20160905	22.3167	47.7166	**70**	20161014	0.150000	65.4333
71	20161117	21.3333	3.65000	**72**	20170102	21.0333	3.35000
73	20170130	7.86667	17.1166	**74**	20170208	19.2667	27.2000
75	20170315	12.2667	62.6500	**76**	20170320	10.3500	15.3833
77	20170527	2.26667	29.5500	**78**	20170710	23.7333	1.53340
79	20170813	10.0500	36.7833	**80**	20171016	13.4500	11.3667

References

Ahlgrimm, M. and R. Forbes (2014). Improving the representation of low clouds and drizzle in the ECMWF model based on ARM observations from the Azores. Month. Weath. Rev. 142, 668-685, doi:10.1175/MWR-D-13-00153.1.

Atmospheric Radiation Measurement (ARM) Climate Research Facility. (1993). updated hourly. Balloon-Borne Sounding System (SONDEWRPR). 2009 to 2017, Eastern North Atlantic (ENA/GRW) Graciosa Island, Azores, Portugal (C1). Compiled by C. Sivaraman, D. Holdridge, D. Troyan, J. Kyrouac, L. Riihimaki, R. Coulter, S. Giangrande, T. Shippert and T. Toto. Atmospheric Radiation Measurement (ARM) Climate Research Facility Data Archive: Oak Ridge, Tennessee, USA. Data set accessed 2017 at http://dx.doi.org/ 10.5439/1150271.

Atmospheric Radiation Measurement (ARM) Climate Research Facility. (2009a). updated hourly. W-band Cloud Radar Active Remote Sensing of Cloud (ARSCLWACR1KOLLIAS). 2009-01-01 to 2010-12-31, ARM Mobile Facility (GRW) Graciosa Island, Azores, Portugal; AMF1 (M1). Compiled by K. Johnson and S. Giangrande. Atmospheric Radiation Measurement (ARM) Climate Research Facility Data Archive: Oak Ridge, Tennessee, USA. Data set accessed 2017 at http://dx.doi.org/ 10.5439/1097547.

Atmospheric Radiation Measurement (ARM) Climate Research Facility. (2009b), updated hourly. Microwave Radiometer (MWRLOS). 2009-01-01 to 2017-12-31, ARM Mobile Facility (GRW) Graciosa Island, Azores, Portugal; AMF1 (M1). Compiled by M. Cadeddu and V. Ghate. Atmospheric Radiation Measurement (ARM) Climate Research Facility Data Archive: Oak Ridge, Tennessee, USA. Data set accessed 2017 at http://dx.doi.org/10.5439/1046211

Atmospheric Radiation Measurement (ARM) Climate Research Facility. (2009c), updated hourly. Ceilometer (CEIL). 2009-01-01 to 2010-12-31, ARM Mobile Facility (GRW) Graciosa Island, Azores, Portugal; AMF1 (M1). Compiled by B. Ermold and V. Morris. Atmospheric Radiation Measurement (ARM) Climate Research Facility Data Archive: Oak Ridge, Tennessee, USA. Data set accessed 2018 at http://dx.doi.org/10.5439/1181954.

Atmospheric Radiation Measurement (ARM) Climate Research Facility. (2013a). updated hourly. Surface Meteorological Instrumentation (MET). 2009 -2010, 2013 to 2017, Eastern North Atlantic (ENA/GRW) Graciosa Island, Azores, Portugal (C1). Compiled by D. Holdridge and J. Kyrouac. Atmospheric Radiation Measurement (ARM) Climate Research Facility Data Archive: Oak Ridge, Tennessee, USA. Data set accessed 2017 at http://dx.doi.org/10.5439/1025220.

Atmospheric Radiation Measurement (ARM) Climate Research Facility. (2013b). updated hourly. Cloud mask from Micropulse Lidar (30SMPLCMASK1ZWANG). 2009 to 2017, Eastern North Atlantic (ENA/GRW) Graciosa Island, Azores, Portugal (C1). Compiled by C. Sivaraman and L. Riihimaki. Atmospheric Radiation Measurement (ARM) Climate Research Facility Data Archive: Oak Ridge, Tennessee, USA. Data set accessed 2017 at http://dx.doi.org/10.5439/1027736.

Atmospheric Radiation Measurement (ARM) Climate Research Facility. (2013c), updated hourly. Ceilometer (CEIL). 2014-08-01 to 2017-12-31, Eastern North Atlantic (ENA) Graciosa Island, Azores, Portugal (C1). Compiled by B. Ermold and V. Morris. Atmospheric Radiation Measurement (ARM) Climate Research Facility Data Archive: Oak Ridge, Tennessee, USA. Data set accessed 2018 at http://dx.doi.org/10.5439/1181954.

Atmospheric Radiation Measurement (ARM) Climate Research Facility. (2014a). updated hourly. Microwave Radiometer, 3 Channel (MWR3C). 2009 to 2017, Eastern North Atlantic (ENA) Graciosa Island, Azores, Portugal (C1). Compiled by M. Cadeddu and V. Ghate. Atmospheric Radiation Measurement (ARM) Climate Research Facility Data Archive: Oak Ridge, Tennessee, USA. Data set accessed 2017 at http://dx.doi.org/10.5439/1025248.

Atmospheric Radiation Measurement (ARM) Climate Research Facility. (2014b), updated hourly. Laser Disdrometer (PARS2). 2014-08-01 to 2017-12-31, Eastern North Atlantic (ENA) Graciosa Island, Azores, Portugal (C1). Compiled by J. Delamere, M. Bartholomew and Y. Shi. Atmospheric Radiation Measurement (ARM) Climate Research Facility Data Archive: Oak Ridge, Tennessee, USA. Data set accessed 2017 at http://dx.doi.org/ 10.5439/1150252.

Atmospheric Radiation Measurement (ARM) Climate Research Facility. (2015). updated hourly. Active Remote Sensing of CLouds (ARSCL) product using Ka-band ARM Zenith Radars (ARSCLKAZRBND1KOLLIAS). 2009-2010, 2015 to 2017, Eastern North Atlantic (ENA/GRW) Graciosa Island, Azores, Portugal (C1). Compiled by K. Johnson, S. Giangrande and T. Toto. Atmospheric Radiation Measurement (ARM) Climate Research Facility Data Archive: Oak Ridge, Tennessee, USA. Data set accessed 2017 at http://dx.doi.org/10.5439/1350630.

Bodas-Salcedo, A., K.D. Williams, P.R. Field, and A.P. Lock (2012). The Surface Downwelling Solar Radiation Surplus over the Southern Ocean in the Met Office Model: The Role of Midlatitude Cyclone Clouds. J. Climat*e,* 25, 7467–7486, doi.org/10.1175/JCLI-D-11-00702.1

Bodas-Salcedo, A., K.D. Williams, M.A. Ringer, I. Beau, J.N. Cole, J. Dufresne, T. Koshiro, B. Stevens, Z. Wang, and T. Yokohata (2014). Origins of the Solar Radiation Biases

over the Southern Ocean in CFMIP2 Models, J. Climate, 27, 41–56, , doi:10.1175/JCLI-D-13-00169.1.

Bretherton, C. S. and M. C. Wyant (1997). Moisture transport, lower-tropospheric stability and decoupling of cloud-topped boundary layers. J. Atmos. Sci. 54, 148-167, doi.org/10.1175/1520-0469(1997)054<0148:MTLTSA>2.0.CO;2

Clothiaux, E. E., T. P. Ackerman, G. G. Mace, K. P. Moran, R. T. Marchand, M. A. Miller, and B. E Martiner (2000). Objective determination of cloud heights and radar reflectivities using a combination of active remote sensors at the ARM CART sites. J. Appl. Meteorol. 39, 645- 665, doi.org/10.1175/1520-0450(2000)039<0645:ODOCHA>2.0.CO;2

Fletcher, J. K., S. Mason and C. Jakob (2016a). The climatology, meteorology and boundary layer structure of marine cold air outbreaks in both hemispheres. J. Climate, 29, 1999-2014, doi:10.1175/JCLI-D-15-0268.1.

Fletcher, J. K., S. Mason and C. Jakob (2016b). A climatology of clouds in marine cold air outbreaks in both hemispheres. J. Climate, 19, 6677-6692, doi:10.1175/JCLI-D-15-0783.1.

Gelaro, R., W. McCarty, M.J. Suárez, R. Todling, A. Molod, L. Takacs, C.A. Randles, A. Darmenov, M.G. Bosilovich, R. Reichle, K. Wargan, L. Coy, R. Cullather, C. Draper, S. Akella, V. Buchard, A. Conaty, A.M. da Silva, W. Gu, G. Kim, R. Koster, R. Lucchesi, D. Merkova, J.E. Nielsen, G. Partyka, S. Pawson, W. Putman, M. Rienecker, S.D. Schubert, M. Sienkiewicz, and B. Zhao (2017). The Modern-Era Retrospective Analysis for Research and Applications, Version 2 (MERRA-2), J. Climate, **30**, 5419-5454, doi.org/10.1175/JCLI-D-16-0758.1

Global Modeling and Assimilation Office (GMAO) (2008). tavg1_2d_slv_Nx: MERRA 2D IAU Diagnostic, Single Level Meteorology, Time Average 1-hourly V5.2.0, Greenbelt, MD, USA, Goddard Earth Sciences Data and Information Services Center (GES DISC), Accessed 2017 at http://dx.doi.org/10.5067/B6DQZQLSFDLH

Haynes, J. M., C. Jakob, W. B. Rossow, G. Tselioudis, and J. Brown (2011). Major characteristics of southern ocean cloud regimes and their effect on the energy budget. J. Climate, 24, 5061-5080, doi:10.1175/2011JCLI4052.1.

Klein S. A. and D. L. Hartmann (1993), The seasonal cycle of low stratiform clouds. J. Climate, 6, 1587-1606.

Köhler, M., M. Ahlgrimm and A. Beljaars (2011). Unified treatment of dry convective and stratocumulus-topped boundary-layers in the ECMWF model. Quart. J. Roy. Meteorol. Soc. 137, 43-57, doi.org/10.1002/qj.713

Kollias, P, E. E. Clothiaux, M. A. Miller, E. P. Luke, K. L. Johnson, K. P. Moran, K. B. Widener, and B. A. Albrecht, (2007). The Atmospheric Radiation Measurement Program cloud profiling radars: second generation sampling strategies, processing and cloud data products, J. Atmos. Ocean. Technol. 24, 1199-1214, doi:10.1175/JTECH2033.1.

Mace, G. G., (2010), Cloud properties and radiative forcing over the maritime storm tracks of the southern ocean and north Atlantic derived from A-train. J. Geophys. Res., 115, D10201, doi:10.1029/2009JD012517.

McCoy, I. L., R. Wood and J. K. Fletcher (2017). Identifying meteorological controls on open and closed mesoscale cellular convection associated with marine cold air

outbreaks. J. Geophys. Res.: Atmospheres, 122, 11678-11702, doi: 10.1002/2017JD027031.

Miyamoto, A., H. Nakamura, and T. Miyasaka, (2018), Influence of the subtropical high and storm track on low-cloud fraction and its seasonality over the South Indian Ocean. J. Climate, 31, 4017-4039, doi:10.1175/JCLI-D-17-0229.1.

Morrison, A. E., S. T. Siems, and M. J. Manton (2011). A three-year climatology of cloud-top phase over the Southern Ocean and north Pacific. J. Climate, 24, 2405-2418, doi:10.1175/2010JCLI3842.1.

Myers, T. A. and J. R. Norris (2013). Observational evidence that enhanced subsidence reduces subtropical marine boundary layer cloudiness. J. Climate, 26, 7507-7524, doi:10.1175/JCLI-D-12-00736.1.

Naud, C.M., J.F. Booth, and A.D. Del Genio (2014). Evaluation of ERA-interim and MERRA cloudiness in the Southern Ocean, J. Climate, 27, 2109-2124, doi:10.1175/JCLI-D-13-00432.1.

Naud, C.M., J.F. Booth, and A.D. Del Genio (2016). The relationship between boundary layer stability and cloud cover in the post-cold frontal region, J. Climate, 29, 8129-8149, doi:10.1175/JCLI-D-15-0700.1.

Pennypacker, S. and R. Wood (2017). a Case study in low aerosol number concentrations over the Eastern North Atlantic: implications for pristine conditions in the remote marine boundary layer. J. Geophys. Res., 122, 12393-12415, doi:10.1002/2017JD027493.

Rémillard, J., P. Kollias, E. Luke, and R. Wood (2012). Marine Boundary Layer Cloud Observations in the Azores. J. Climate, 25, 7381–7398, doi.org/10.1175/JCLI-D-11-00610.1

Tselioudis G., Y. Zhang and W. B. Rossow (2000), Cloud and radiation variations associated with northern midlatitude low and high sea level pressure regimes. J. Climate, 13, 312-327.

Wang, Z. and K. Sassen (2001). Cloud type and macrophysical property retrieval using multiple remote sensors. J. App. Meteorol. 40, 1665-1682, doi.org/10.1175/1520-0450(2001)040<1665:CTAMPR>2.0.CO;2.

Wood, R. (2012). Stratocumulus Clouds, Mon. Weather Rev., 140, 2373–2423, doi.org/10.1175/MWR-D-11-00121.1.

Wood, R. and C.S. Bretherton (2006), On the Relationship between Stratiform Low Cloud Cover and Lower-Tropospheric Stability. J. Climate, 19, 6425–6432, doi.org/10.1175/JCLI3988.1.

Wood, R., and Coauthors (2015), Clouds, aerosols, and precipitation in the marine boundary layer: An ARM Mobile Facility deployment, Bull. Amer. Meteor. Soc., 96, 419–440, doi.org/10.1175/BAMS-D-13-00180.1

Zhao and co-authors (2018), The GFDL Global Atmosphere and land model AM4.0/LM4.0 – Part II: Model description, sensitivity studies and tuning strategies. J. Adv. Model. Earth Syst. in press, doi: 10.1002/2017MS001209.

Table 1. List of each environmental metric considered here, with formula/symbol, dataset used for its evaluation in the analysis, expected impact on cloud boundaries based on previous work in subtropical regions, and with examples of references.

Metric	**Symbol/formula**	**Datasets used**	**Expected impact for increase in metric**	**Previous analyses**
Subsidence strength	ω	MERRA-2	Decrease in cloud base, top and extent	Myers and Norris (2013)
Surface wind speed	-	meteorological station	Both act as proxy for surface turbulent fluxes based on bulk formula. Increase in cloud base, top and extent	Miyamoto et al. (2018)
Sea-air temperature contrast	$\Delta T_{surf} = T_{skin}-T_{air}$	Skin temperature T_{skin} from MERRA-2 and the surface air temperature T_{air} from the meteorological station		Miyamoto et al. (2018); McCoy et al. (2017)
Estimated Inversion strength (Wood and Bretherton, 2006)	$EIS = \theta_{700} - \theta_{surf} - \Gamma_m^{850}(Z_{700}-LCL)$	Radiosonde, meteorological station	Decrease in cloud base, top, extent	Wood (2012), Myers and Norris (2013); McCoy et al. (2017)
MCAO parameter M (Fletcher et al. 2016a)	$M = \theta_{skin}-\theta_{800hPa}$	MERRA-2 for θ_{skin}, radiosonde for θ_{800hPa}	Increase in cloud base, top, extent	Fletcher et al. (2016b); McCoy et al. (2017)
Surface relative humidity	RH_{surf}	Meteorological station	Decrease in cloud-base height	Wood (2012)
Precipitable Water	PW	MERRA-2 and MWR	Increase in LWP	Wood (2012)

Table 2. Correlation coefficient between cloud parameters and large scale metrics averaged in fixed size bins for each metric in PCF / *non-PCF-north (non-PCF-south)* periods. The coefficients marked in bold indicate a significance t-test of better than 99.95% confidence that the relationship is linear. The coefficients marked with * are significant to better than 99% confidence.

Metrics	ARSCL Cloud-base Height	ARSCL Cloud-top Height	ARSCL Cloud-top Temperature	ARSCL Vertical Extent	MWR Log LWP
EIS	-0.61 / ***-0.81 (-0.90)***	-0.83 / ***-0.84 (-0.89)***	**0.90** / ***0.84 (0.79)***	-0.74 / *-0.39 (-0.30)*	-0.50 / *0.39 (-0.48)*
ΔT_{surf}	0.53 / *0.48 (0.61)*	0.78 / ***0.92*** *(0.42)*	**-0.95** / ***-0.93*** *(-0.75)*	0.59 / ***0.91*** *(0.19)*	**0.87** / *0.06 (-0.46)*
Wind speed	0.33 / *0.53 (-0.51)*	0.69/ ***0.77*** *(0.04)*	**-0.83** / ***-0.91*** *(0.09)*	0.62 / *0.63 (0.58)*	0.62 / *0.22 (-0.38)*
M	**0.99** / ***0.95 (0.97)***	**0.97**/ ***0.97 (0.97)***	**-0.95** / ***-0.95*** *(-0.90)*	0.66 / *0.69 (0.84)*	0.71* / *-0.47 (-0.46)*
ω	0.49 / *0.63 (0.16)*	0.51 / ***0.78*** *(0.37)*	-0.73 / ***-0.91 (-0.82)***	0.09 / *0.44 (0.19)*	0.09 / *0.08 (0.15)*
RH_{surf}	**-0.99** / ***-0.94 (-0.96)***	-0.76 / ***-0.92*** *(-0.87)*	0.84 / ***0.94 (0.96)***	**0.80** / *0.86 (0.84)*	0.67 / *0.60 (0.67)*
PW	-0.85 / ***-0.91 (-0.82)***	**-0.95** / ***-0.83*** *(-0.55)*	**0.97** / ***0.97 (0.94)***	-0.02 / *0.48 (0.45)*	-0.01 / *0.35* ***(0.70)***

Table 3. Relationship between ceilometer cloud-base height, MPL cloud-top height and MPL cloud-top temperature and large scale metrics: correlation coefficients for PCF / *non-PCF-north* periods. The coefficients marked in bold indicate a significance t-test of better than 99.95% confidence that the relationship is linear. Highlighted in grey are those relationships that are as strong or stronger than in Table 2.

Metrics	Ceilometer Cloud-base Height	MPL Cloud-top Height	Cloud-top Temperature MPL
EIS	-0.69 / *-0.73*	**-0.95** / ***-0.91***	**0.93** / ***0.88***
ΔT_{surf}	0.81 / *0.49*	0.84 / *0.77*	**-0.97** / ***-0.94***
Wind speed	0.55 / *0.16*	**0.80**/ *0.51*	**-0.92** / ***-0.87***
M	**0.92** / ***0.84***	**0.93**/ ***0.97***	**-0.95** / ***-0.98***
ω	0.60 / *0.58*	0.57 / *0.68*	-0.75 / ***-0.81***
RH_{surf}	**-0.96** / ***-0.94***	-0.82 / *-0.65*	**0.90** / ***0.91***
PW	-0.87 / ***-0.95***	**-0.90** / *-0.56*	**0.97** / ***0.93***

Table 4. Correlation coefficients between M and all other large-scale metrics averaged into fixed size bins for the parameters in the first column for PCF, non-PCF-north and non-PCF-south periods. The coefficients marked in bold indicate a significance t-test of better than 99.95% confidence that the relationship is linear.

Parameters sorted in fixed size bins	**M -PCF**	**M- Non-PCF-north**	**M – Non-PCF-south**
EIS	**-0.98**	**-0.98**	**-0.96**
Wind speed	0.80	**0.83**	0.30
PW	-0.90	**-0.88**	**-0.72**
ω	0.50	**0.81**	0.65
ΔT_{surf}	0.81	**0.85**	0.54
RH_{surf}	-0.87	-0.78	-0.78

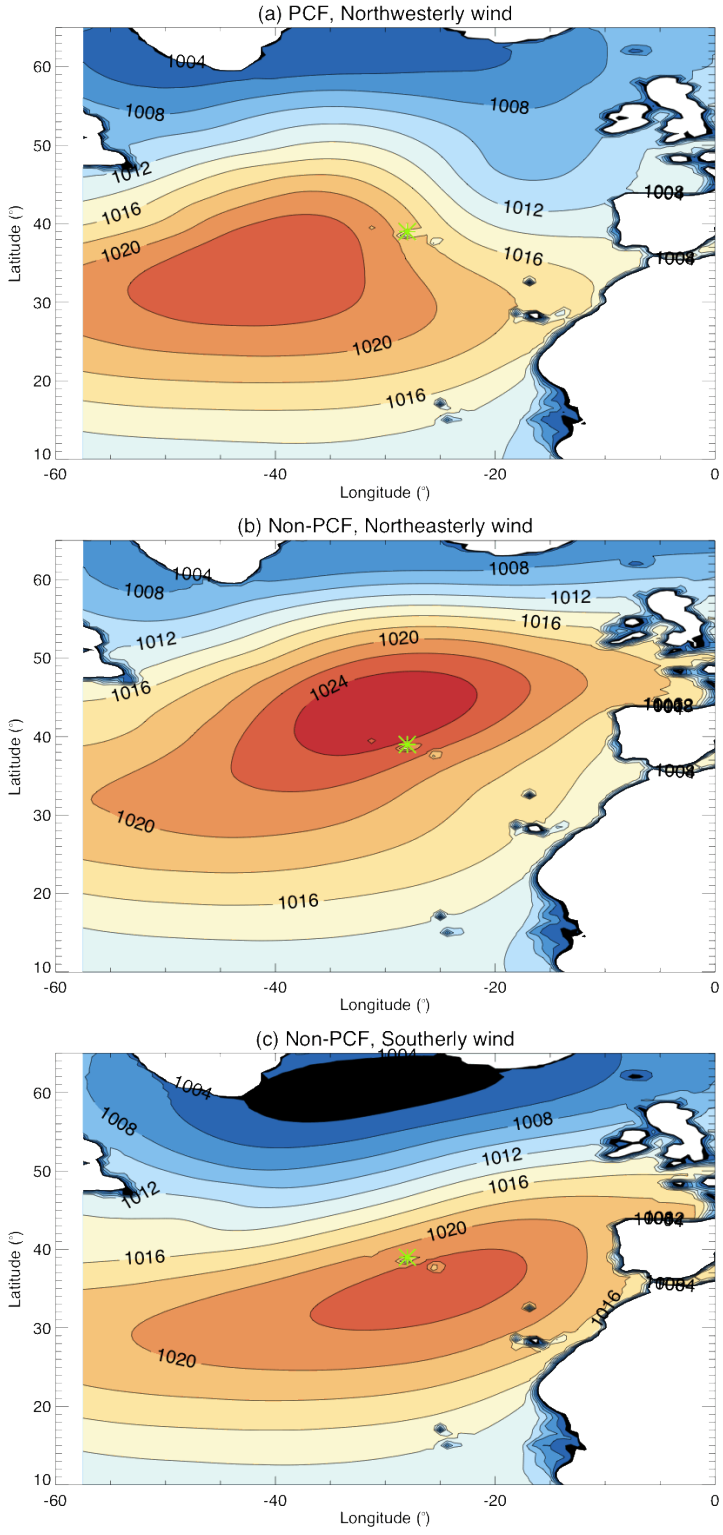

Figure 1. MERRA-2 hourly SLP composites for (a) post-cold frontal periods, (b) non-PCF northeasterly wind, and (c) non-PCF periods with southerly wind, identified at the time of the radiosonde launches. The green star indicates the location of the ENA site.

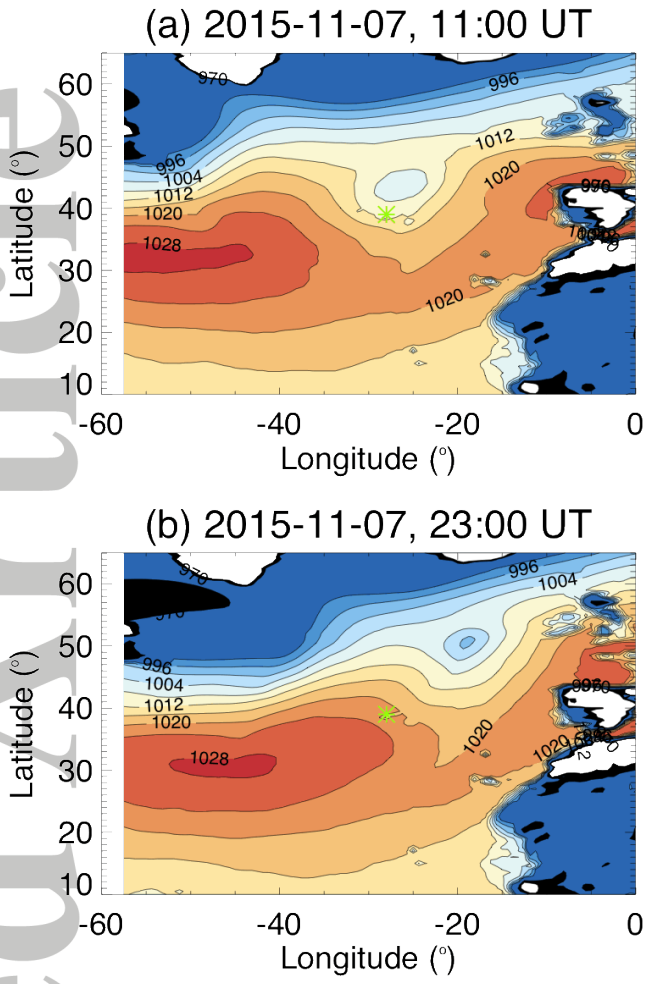

Figure 2. Surface pressure maps of the ENA region (green star) on 2015-11-07, at (a) 11:00 UT as a cold front is about to pass over the site and (b) 23:00 UT when the cold front has passed, the wind is still northwesterly but the site is now under the influence of an incoming high pressure system.

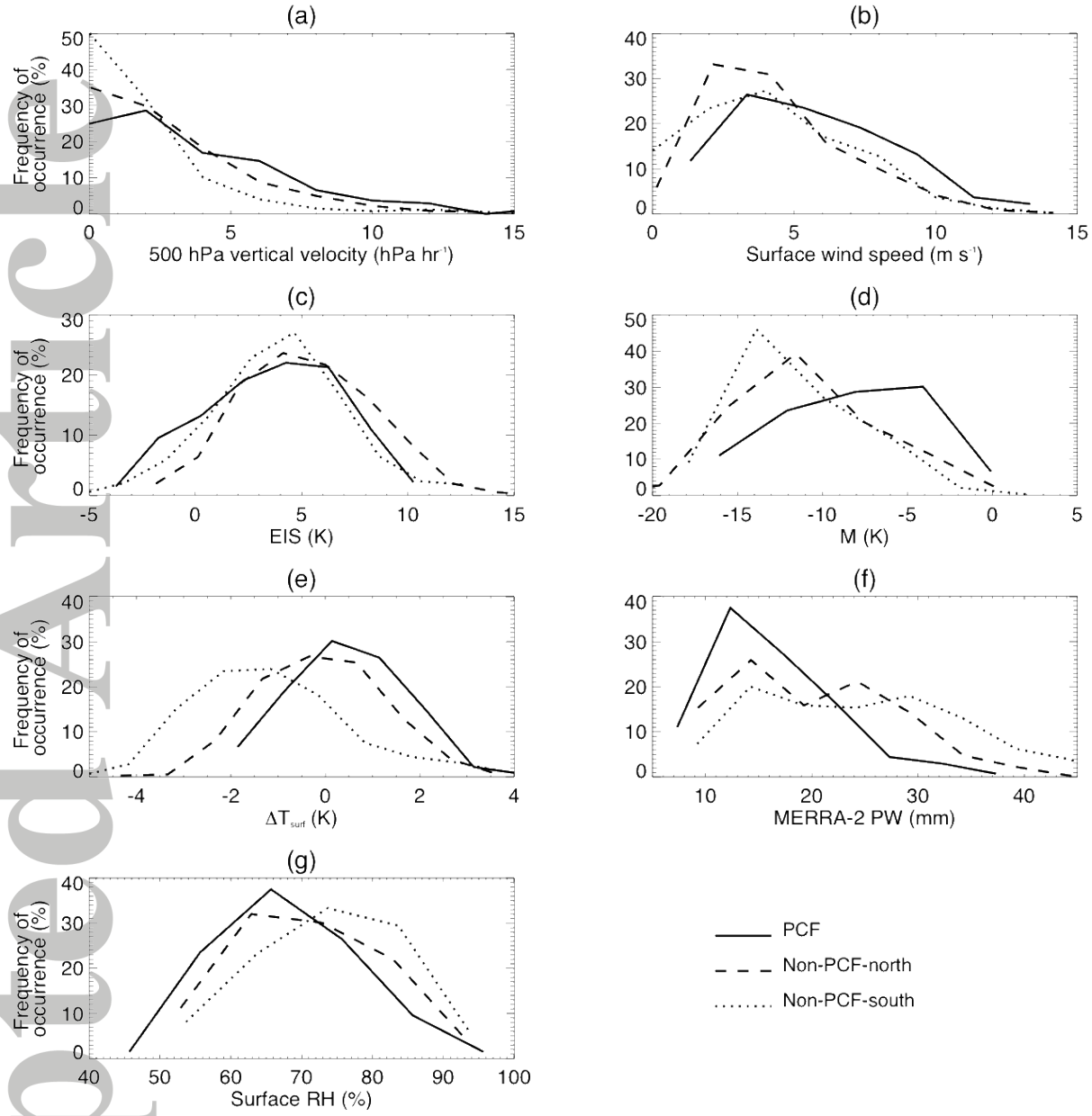

Figure 3. Distribution of (a) 500 hPa vertical velocity, (b) surface wind speed, (c) EIS, (d) M, (e) ΔT_{surf}, (f) MERRA-2 PW, (g) RH_{surf} in PCF (solid), non-PCF-north (dashed) and non-PCF-south (dotted) periods.

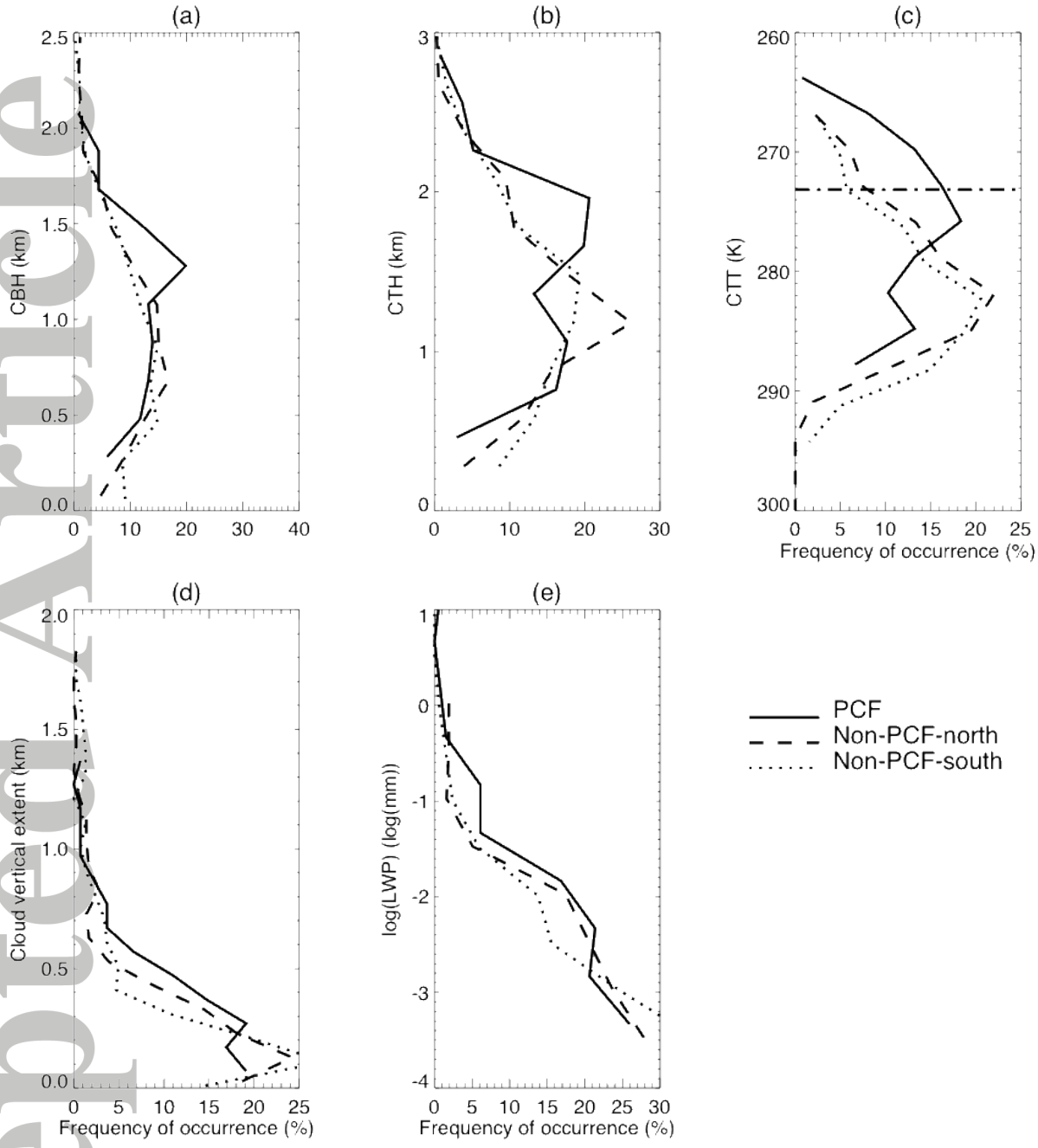

Figure 4. Histograms of ARSCL (a) cloud-base height, (b) cloud-top height, (c) cloud-top temperature, (d) cloud vertical extent and (e) logarithm of MWR LWP for PCF (solid), non-PCF-north (dashed) and non-PCF-south (dotted) periods. The horizontal dot-dashed line in (c) marks the location of 273.15 K.

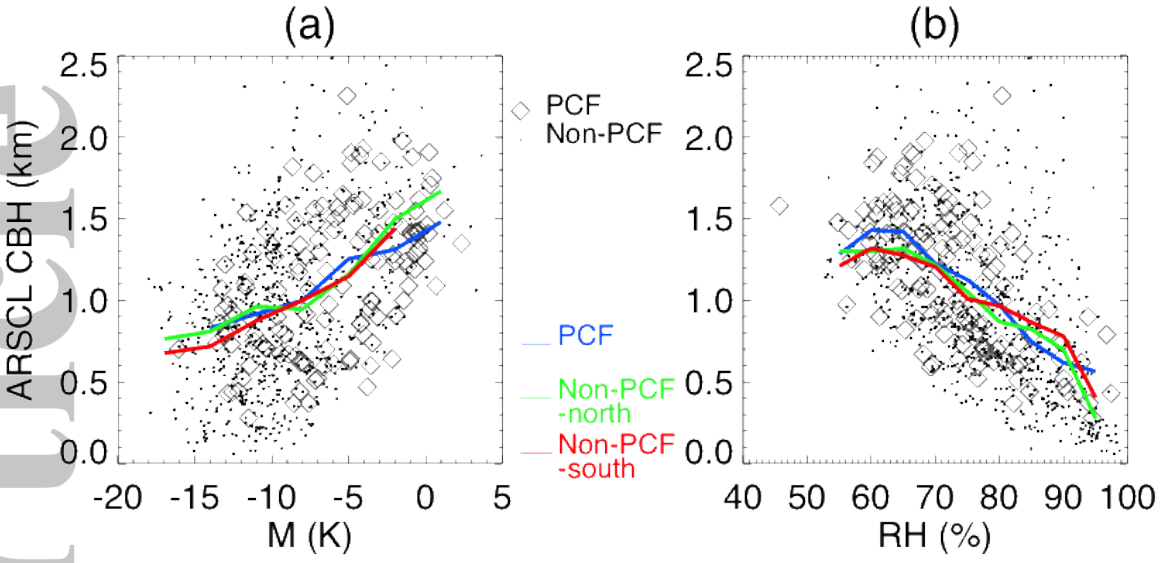

Figure 5. Cloud-base height retrieved with ARSCL as a function of (a) M and (b) RH_{surf} for PCF (black diamonds) and non-PCF (black dots) periods. The mean for fixed size bins of M and RH_{surf} are shown with solid lines for PCF (blue), non-PCF-north (green) and non-PCF-south (red).

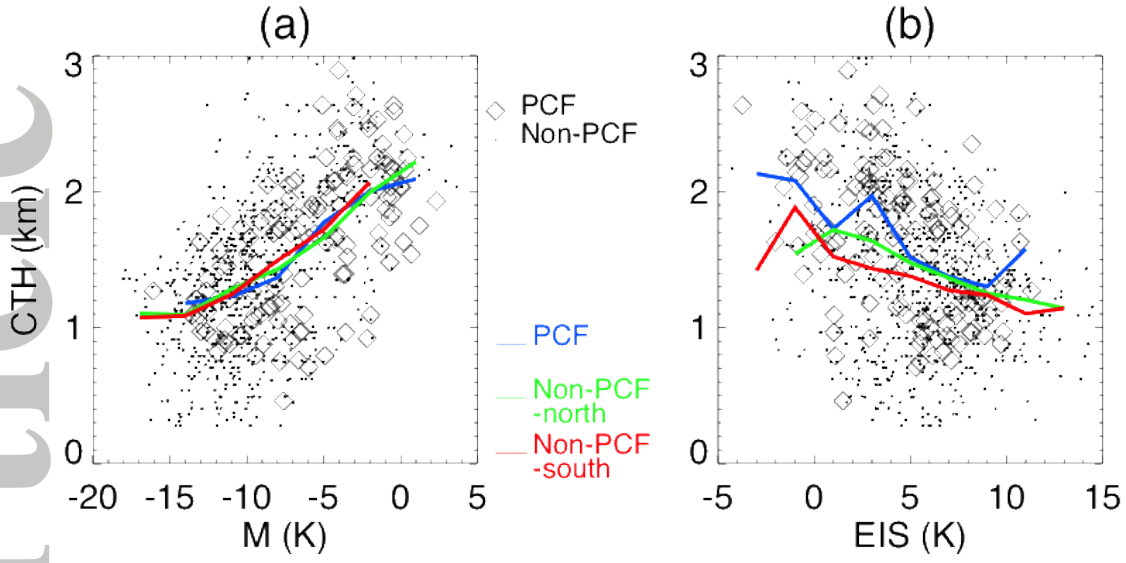

Figure 6. Cloud-top height retrieved with ARSCL as a function of (a) M and (b) EIS for PCF (black diamonds) and non-PCF (black dots) periods. The mean for fixed size bins of M and RH_{surf} are shown with solid lines for PCF (blue), non-PCF-north (green) and non-PCF-south (red).

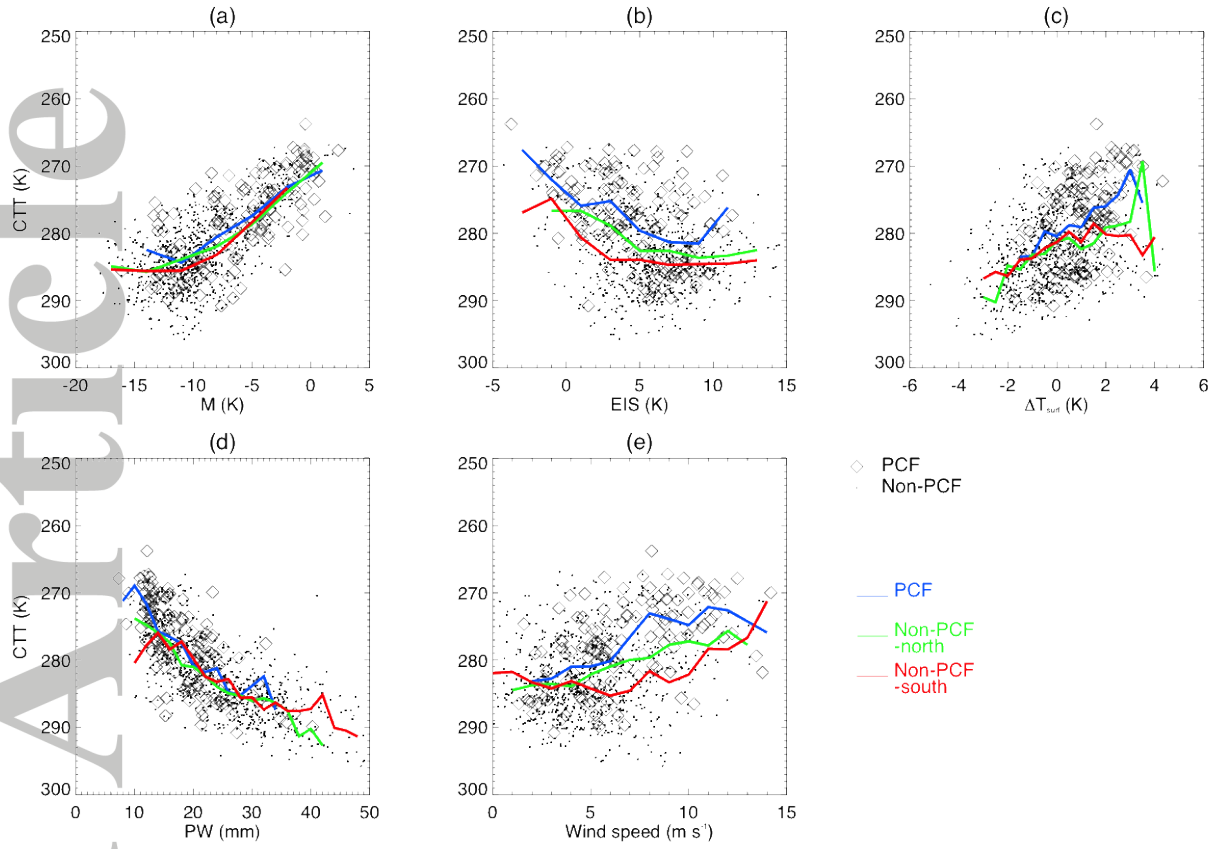

Figure 7. Cloud-top temperature retrieved with ARSCL as a function of (a) M, (b), EIS, (c) ΔT_{surf}, (d) PW and (e) surface wind speed for PCF (black diamonds) and non-PCF (black dots) periods. The mean for fixed size bins of M, EIS, ΔT_{surf}, PW and wind speed are shown with solid lines for PCF (blue), non-PCF-north (green) and non-PCF-south (red).

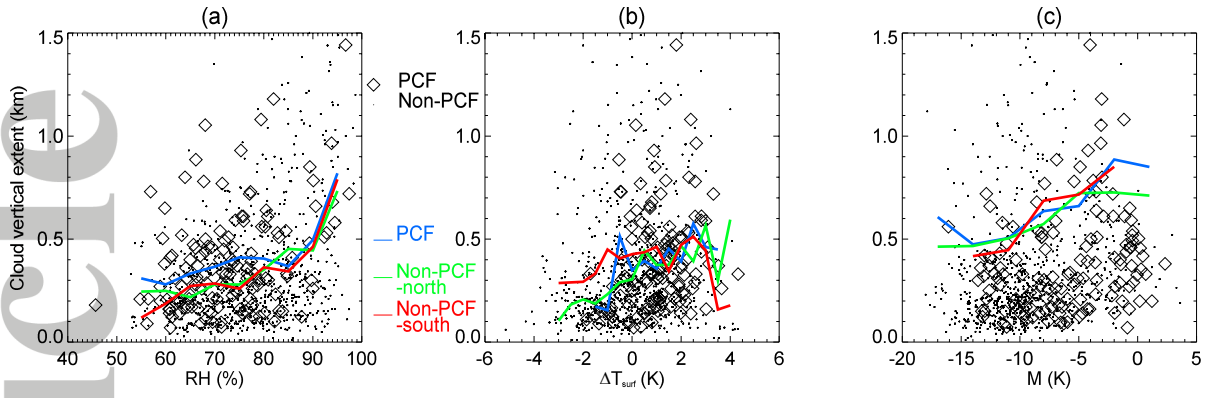

Figure 8. Cloud vertical extent obtained with ARSCL as a function of (a) RH_{surf}, (b) ΔT_{surf} and (c) M for PCF (black diamonds) and non-PCF (black dots) periods. The mean for fixed size bins of RH_{surf}, ΔT_{surf} and M are shown with solid lines for PCF (blue), non-PCF-north (green) and non-PCF-south (red).

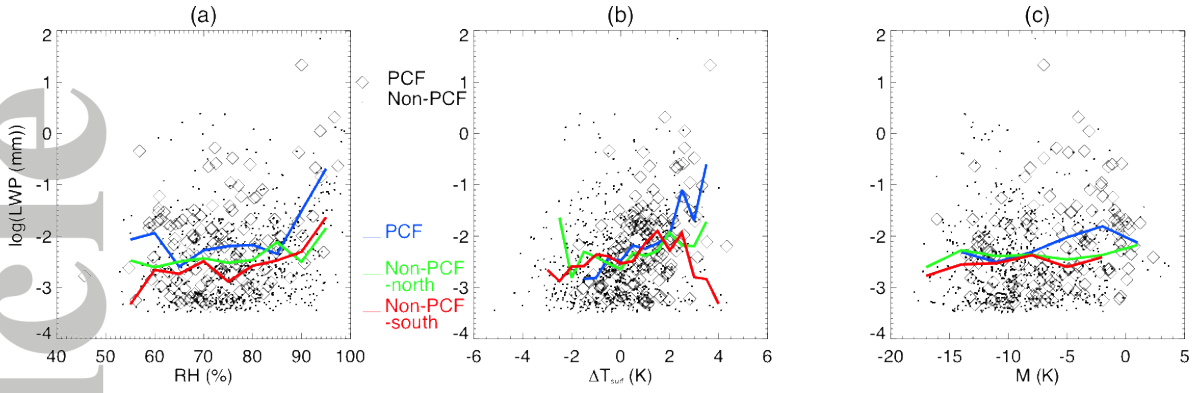

Figure 9. Logarithm of cloud liquid water path retrieved with MWR as a function of (a) RH_{surf}, (b) ΔT_{surf}, and (c) M for PCF (black diamonds) and non-PCF (black dots) periods. The mean for fixed size bins of RH_{surf}, ΔT_{surf} and M are shown with solid lines for PCF (blue), non-PCF-north (green) and non-PCF-south (red).

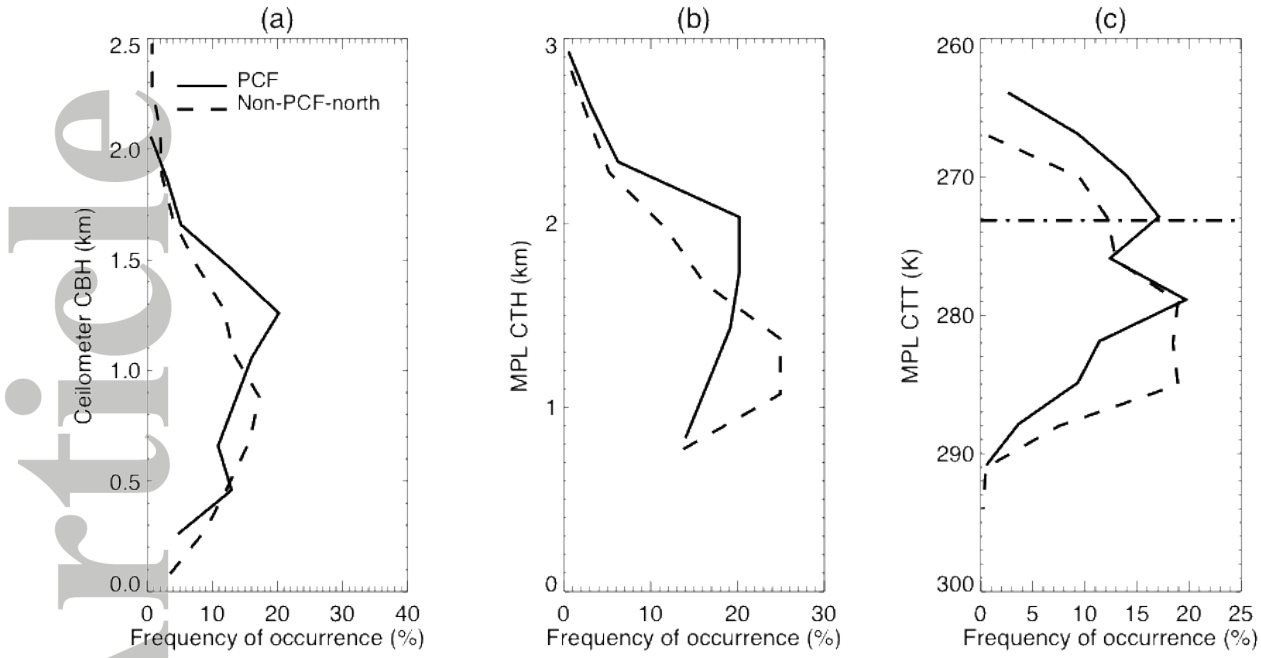

Figure 10. Histograms of (a) ceilometer cloud-base height, (b) MPL cloud-top height, and (c) MPL cloud-top temperature for PCF (solid), and non-PCF-north (dashed) periods. The horizontal dot-dashed line in (c) marks the location of 273.15 K.